50th AIAA Aerospace Sciences Meeting including the New Horizons Forum and Aerospace Exposition
09 - 12 January 2012, Nashville, Tennessee
AIAA 2012-1104

On the Compressible Bidirectional Vortex. Part 2: A Beltramian Flowfield Approximation

Brian A. Maicke* and Joseph Majdalani†
University of Tennessee Space Institute, Tullahoma, TN 37388, USA

In the first part of this paper series, a compressible Bragg-Hawthorne framework is developed in the form of a density-stream function formulation that may be applied to a wide class of steady, axisymmetric flow problems. In this sequel, the procedure is implemented with the aim of retrieving an approximate compressible solution to describe the helical motion observed in a cyclonic, bidirectional vortex chamber. Our approach centers on sequentially solving the linearized density-stream function relations to the extent of producing a closed-form expression for the compressible, swirl-dominated motion. This effort begins by conceiving a judicious set of boundary conditions that may be paired with the Bragg-Hawthorne procedure established previously. Then using a Rayleigh-Janzen expansion of the resulting system of partial differential equations, a solution is achieved at the leading and first orders in the injection Mach number squared. At the leading order, the incompressible approximation of the linear Beltramian flowfield is recovered, with compressibility effects relegated to the first order. In moving to higher orders, our approach requires the numerical integration of several groups of Bessel functions. These are specified individually as special functions that enable us to retain the analytical character of the first-order correction. Among significant findings predicted by this model, an appreciable steepening of the axial velocity profile is captured, thus mirroring a similar mechanism observed in solid rocket motors (SRMs). Furthermore, the mantle location, which is ordinarily committed to a single radial location in the absence of compressibility, gains an axial dependence that is reminiscent of the radial shifting of mantles reported in some experimental trials and numerical simulations. This sensitivity becomes more pronounced at higher injection Mach numbers and ratios of specific heats. The sensitivity of the solution to variations in κ, the inflow swirl parameter, is also investigated. We find that increasing κ leads to relative growth in both the incompressible and compressible velocities in the axial and radial directions. Conversely, at small values of κ, i.e. when the axial and radial velocities are overwhelmingly dominated by the tangential motion, the compressible solution approaches the leading-order result. Albeit counter-intuitive at first, imparting a progressively larger swirl component stands to promote the axisymmetric distribution of flowfield properties, and these include an implicit resistance to compression in the tangential direction, lest axisymmetry is violated. As for the density, its largest excursions occur near the centerline, and these become more appreciable at higher Mach numbers and ratios of specific heats. From a broader perspective, this study not only provides a viable approximation to the linear Beltramian motion associated with the classic cyclonic flowfield, it also offers a proof-of-concept of the procedure introduced by the authors in their companion article. Specifically, the present analysis confirms the validity of the newly established compressible Bragg-Hawthorne framework in the treatment of swirl-driven and other axisymmetric fluid motions.

Nomenclature

a	chamber radius
A_i	inlet area
B	tangential angular momentum, rv
b	open radius
c_0	reference speed of sound, $\sqrt{\gamma R_0 T_0}$
H	stagnation enthalpy or total pressure head
L	chamber length
l	aspect ratio, L/a
M_0	reference Mach number, U/c_0
M_W, R_u	molecular weight and universal gas constant
$\dot{m}_i$	inlet mass flow rate
p	pressure

*Graduate Research Assistant, Department of Mechanical, Aerospace and Biomedical Engineering. Member AIAA.
†H. H. Arnold Chair of Excellence in Advanced Propulsion and Professor, Department of Mechanical, Aerospace and Biomedical Engineering. Associate Fellow AIAA. Fellow ASME.

$\bar{Q}_i$	inlet volumetric flow rate, UA_i
R_0	reference gas constant, R_u/M_W
r	radial coordinate
T_0	reference temperature
t	time
$\boldsymbol{u}$	velocity vector, (u, v, w)
U	mean injection velocity
z	axial coordinate

Greek

β	open radius fraction, b/a
γ	ratio of specific heats
ν	kinematic viscosity
ρ	density
$\boldsymbol{\Omega}$	vorticity vector
ψ	stream function

Subscripts and Symbols

0, i, o	reference, inlet, or outlet property
$0, 1, 2, \ldots$	perturbation order
$\bar{}$	overbars designate dimensional quantities

Abbreviations and Acronyms

BHE	Bragg-Hawthorne equation
ODE	ordinary differential equation
PDE	partial differential equation
SRM	solid rocket motor
VCCWC	Vortex Combustion Cold-Wall Chamber

I. Introduction

Swirling flows continue to serve as an appealing topic of research due to their interesting characteristics and overarching applications. For example, elements of unconfined vortex dynamics have been used to explain intriguing mechanisms associated with natural phenomena observed in hurricanes, cyclones, twisters, dust devils and typhoons.[1] Such relations have also been employed to describe the large scale formation, pinwheel motion, and helical expansion of galaxies.[2,3] In aerodynamics, vortex modeling plays a key role in both fixed and rotating wing aircraft design. In more direct industrial settings, centrifugal flow separators, vortex-fired combustors, cyclonic boilers, and spiral-flow vacuum cleaners are merely a few of the devices that incorporate swirl at the basis of their operation.[4–6]

In what pertains to confined vortex research, an extensive body of literature exists, with a primary concentration on the experimental testing discipline in the context of cyclone separators. Early experiments, such as those by ter Linden,[7] were concerned with improving the efficiency of the separator. Additional early investigations[8–10] provided vital insights into the qualitative features of confined vortex motions, noting the ubiquitous presence of a forced core near the vortex center of rotation. This distinguishing characteristic was absent in most external, naturally occurring swirling patterns that were routinely modeled as free, irrotational, vortex structures with tangential velocities that decayed with the inverse distance from their epicenter.

Along with the tremendous leap in computational capabilities, research trends followed suit by shifting away from experimentation in favor of numerical simulation. In this vein, a variety of computational programs emerged and these sought to cover a broad band of confined vortex applications. Some noteworthy investigations included those by Hoekstra, Derksen and van den Akker,[11] Fang, Majdalani and Chiaverini,[12] Rom, Anderson and Chiaverini,[13] Hu *et al.*,[14] and Zhiping, Yongje and Qinggang,[15] among others. However, despite their attempt at covering an array of modeling approaches, only a few of these studies offered results that extended beyond the scope of the individual problems that they tackled.

When compared to the available experimental and numerical literature, theoretical models of confined vortex flows, especially those in multiple dimensions, stand by far as the least available or well advanced, and this may be attributed

in part to the multiple layers of complexities that may be entailed in their development. An often cited study by Bloor and Ingham[16] considers a form of the Bragg-Hawthorne equation in spherical coordinates to construct a theoretical model for conical separators. Their approximation is revisited by Barber and Majdalani[17] who turn it into an exact solution to Euler's equations. Apart from these studies, much of the theoretical work encountered in the literature relies on semi-empirical techniques, with parameters originating almost exclusively from experimental data.[18]

Prompted by this relative dearth of analytical models, Vyas and Majdalani[19] initiated the development of an inviscid model of the bidirectional vortex in the context of a propulsive application.[20] Over time, their model was refined to include increasingly more realistic effects. For example, a treatment of the viscous core was first added,[21] followed by a characterization of multidirectionality and possible formation of multiple mantles.[22] The sidewall boundary layers were also examined by Majdalani and Chiaverini[23] along with Batterson and Majdalani,[24] while a compressible analog with a viscous core was conceived by Maicke and Majdalani.[25] At the heart of these approaches stood the vorticity-stream function approach, an extended form of the classical technique that relates the vorticity to the stream function by way of the vorticity transport equation. The resulting framework facilitates the quest for exact or approximate solutions given judicious assumptions and a well-conceived assortment of meaningful boundary conditions.

In the interest of achieving a more comprehensive confined vortex formulation, Majdalani[26] and, similarly, Barber and Majdalani[17] have revisited the Bragg-Hawthorne equation in cylindrical and spherical coordinates, respectively. Their approach utilizes the stream function approach, but rather than rely on the vorticity transport equation for closure, theirs leverages the conserved forms of the stagnation pressure head and angular momentum. As both of these quantities may be expressed in terms of the stream function, a relation may be obtained uniquely for the stream function in which all other unknowns are eliminated. Subsequently, appropriate guesses may be selected for the pressure head and angular momentum along with a suitable group of auxiliary conditions.

In an effort to extend Majdalani's incompressible Beltramian models,[26] and by way of illustrating the versatility of the compressible Bragg-Hawthorne framework derived in Part 1, this sequel will concentrate on the bidirectional vortex. This particular model is used to describe the bulk gaseous motion in the Vortex Combustion Cold Wall Chamber (VCCWC) depicted in Fig. 1. In this configuration, fluid is injected tangentially to the inner circumference, just upstream of the nozzle base, and then spirals along the outer portion of the chamber. The flow reaches the headwall and reverses axial direction, swirling back through the inner region till existing across the partially open base. Using this helical flowpath helps to insulate the sidewalls of the combustion chamber against the high-temperature combustion products. These are generally confined to the core, outflow region.

In Part 1 of this series,[29] we discussed the general form of the compressible extension to the Bragg-Hawthorne equation. In this sequel, the density-stream function procedure associated with the compressible BHE framework will be applied to the bidirectional vortex. Naturally, the present model will exhibit features that mirror those used by Majdalani,[26] especially regarding the fundamental flow assumptions and the overall selection of the angular momentum and stagnation enthalpy terms. The expanded compressible equations will then be solved using the Rayleigh-Janzen perturbation technique. This procedure has been developed in multiple dimensions and refined by Majdalani,[30] and Maicke and Majdalani,[31] in axisymmetric and planar configurations, respectively. In this vein, both leading and first-order equations will be perturbed in the reference Mach number squared before undergoing a systematic procedure aimed at extracting a compressible correction to the Beltramian class of bidirectional vortex motions. In closing, results will be compared to the incompressible case and to one another for increasing injection Mach numbers, ratios of specific heats, and inflow swirl parameters.

II. Problem Formulation

A. Compressible Bragg-Hawthorne Framework

In Part 1 of this series,[29] the compressible Bragg-Hawthorne framework was established and perturbed using the Rayleigh-Janzen expansion technique. For the reader's convenience, the essential stream function equations entailed in this model are reproduced below:

$$O(1): D^2\psi_0 + B_0^2\psi_0 = 0 \tag{1}$$

$$O(M_0^2): D^2\psi_1 + B_0\psi_1 = \frac{\partial\rho_1}{\partial z}\frac{\partial\psi_0}{\partial z} + \frac{\partial\rho_1}{\partial r}\frac{\partial\psi_0}{\partial r} - \rho_1\left(D^2\psi_0 + 3B_0^2\psi_0\right) - B_2\psi_0 - B_3\psi_0^3 \tag{2}$$

As part of this framework, the sequential evaluation of density relations is required. The corresponding system includes:

$$O(1): \frac{\gamma+1}{\gamma-1}\rho_1 = -\frac{1}{2r^2}\left[\left(\frac{\partial\psi_0}{\partial r}\right)^2 + \left(\frac{\partial\psi_0}{\partial z}\right)^2 + B_0^2\psi_0^2\right] \tag{3}$$

$$O(M_0^2): \frac{\gamma+1}{\gamma-1}\left(\rho_2 + \gamma\rho_1^2\right) = -\frac{B_0^2\psi_0}{r^2}\left(\rho_1\psi_0 + \psi_1\right) - \frac{1}{2r^2}\left(\frac{\partial\psi_0}{\partial r}\frac{\partial\psi_1}{\partial r} + \frac{\partial\psi_0}{\partial z}\frac{\partial\psi_1}{\partial z} + B_2\psi_0^2 + B_3\psi_0^4\right) \tag{4}$$

Equations (1)-(4) enable us to emulate the strategies used by Bloor and Ingham[16] and Majdalani.[26] Specifically to our case, we posit:

$$\frac{\mathrm{dH}}{\mathrm{d}\psi} = 0; \quad \mathrm{B} = \sqrt{B_0^2\psi^2 + B_1^2 + M_0^2\psi^2\left(B_2^2 + \tfrac{1}{2}B_3^2\psi^2\right)}; \quad \frac{\mathrm{dB}}{\mathrm{d}\psi} = \frac{B_0^2\psi + M_0^2\psi\left(B_2^2 + B_3^2\psi^2\right)}{\sqrt{B_0^2\psi^2 + B_1^2 + M_0^2\psi^2\left(B_2^2 + \tfrac{1}{2}B_3^2\psi^2\right)}} \tag{5}$$

It may be instructive to note that Eq. (5) represents only one possible combination leading to a physical solution of the Bragg-Hawthorne equation. Evidently, other forms of B and H may be contrived to precipitate different results. Nonetheless, other varieties are more likely to produce analytically intractable problems, or to numerical solutions that may not be entirely physical.

B. The Bidirectional Vortex

As alluded to earlier,[29] the motivation for the present study centers on the bidirectional vortex flowfield that is relevant to a number of cyclonic-flow applications, including the VCCWC engine prototype. In its basic form, the VCCWC may be modeled as a closed-open cylinder of radius a and height L. When all spatial coordinates are normalized by the radius, an idealized chamber of unit radius emerges, as depicted in Fig. 2. The origin of the

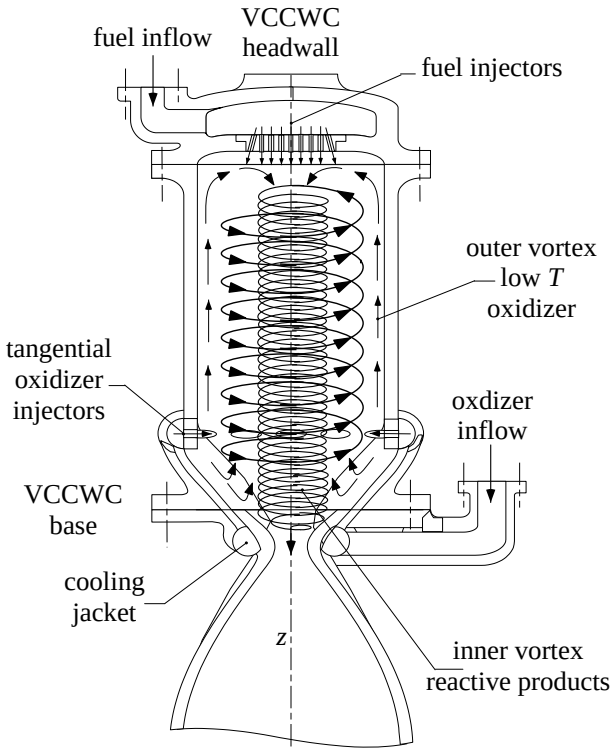

Figure 1. Schematic of the Vortex Combustion Cold-Wall Chamber (VCCWC) in which the inner and outer vortex regions are identified.[27,28]

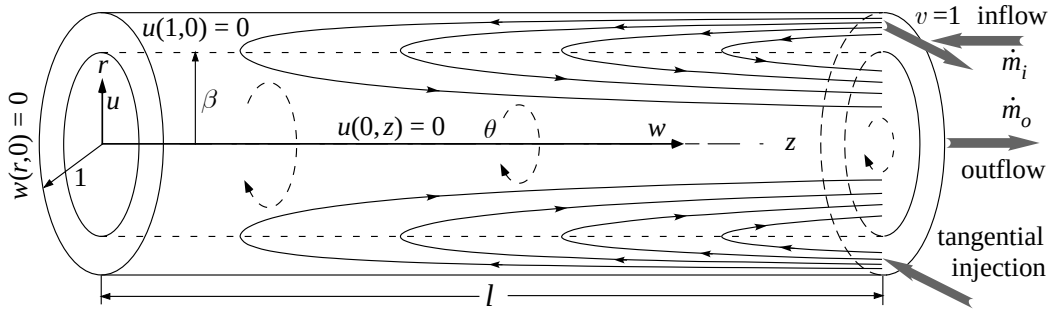

Figure 2. Dimensionless coordinates and key parameters associated with the mathematical idealization of the bidirectional vortex chamber.

coordinate system may be conveniently placed a the center of the headwall with the dimensionless radial and axial coordinates being r and z, respectively. The chamber contains a confined vortex that is dominated by its swirl velocity, U; the latter may be used to normalize all velocities to the extent of producing a unit tangential velocity at the inlet ($v = 1$). In practice, this average inflow velocity is induced by tangential injectors that are evenly distributed around the engine base, just upstream of the nozzle. Due to unavoidable collisions at the boundaries, the fluid develops both axial and radial components of velocity as it swirls towards the headwall while occupying the outer, annular region. When the flow reaches the headwall, it reverses axial direction and returns along the chamber bore until making its exit through the partially open base of radial fraction β. As usual, a spinning, non-translating mantle separates the two vortex regions. In its simplest mathematical idealization, two geometric parameters emerge in the analysis:[19] the aspect ratio $l = L/a$ and the open radial fraction at the base, $\beta = b/a$. The latter is often taken to coincide with the mantle location in such a manner to allow the outflow diameter to match that of the outlet cross-section. The resulting scenario is captured in Fig. 2 where the broken lines of radius β delineate the interfacial boundary between the inner, core and outer, annular vortex regions. Such optimal configuration mitigates the onset of flow collisions and the establishment of undesirable recirculation zones.

In modeling the bidirectional vortex, the following boundary conditions are customarily adopted:

- No axial flow at the headwall.
- No radial flow across the centerline.
- No radial flow at the sidewall.
- Inlet and exit mass flow rates coincide.

As depicted on the graph in dimensionless form, these conditions translate into

$$w(r,0) = 0;\ \frac{1}{\rho r}\frac{\partial \psi}{\partial r} = 0 \tag{6}$$

$$u(0,z) = 0;\ -\frac{1}{\rho r}\frac{\partial \psi}{\partial z} = 0 \tag{7}$$

$$u(1,z) = 0;\ -\frac{1}{\rho r}\frac{\partial \psi}{\partial z} = 0 \tag{8}$$

and

$$\dot{m}_i = 2\pi \int_0^\beta \rho\, \boldsymbol{u}\cdot\boldsymbol{n}\, r\, \mathrm{d}r \tag{9}$$

To remain consistent with the Rayleigh-Janzen perturbation technique, the boundary conditions must also be expanded in terms of the Mach number squared. Following the procedure outlined in Part 1,[29] the leading-order constraints are

found to be

$$w_0(r,0) = 0;\ \frac{1}{r}\frac{\partial \psi_0}{\partial r} = 0 \tag{10}$$

$$u_0(0,z) = 0;\ -\frac{1}{r}\frac{\partial \psi_0}{\partial z} = 0 \tag{11}$$

$$u_0(1,z) = 0;\ -\frac{1}{r}\frac{\partial \psi_0}{\partial z} = 0 \tag{12}$$

and

$$Q_i = 2\pi \int_0^\beta w_0\ r\ \mathrm{d}r = 2\pi \int_0^\beta \frac{\partial \psi_0}{\partial r}\ \mathrm{d}r \tag{13}$$

In the above, the incompressible boundary conditions used by Majdalani[26] are restored identically.

In conformance with perturbation theory, the boundary conditions at the first (compressible) order must not unduly influence the incompressible motion. To ensure that the solution remains valid $\forall M_0$, a set of homogeneous boundary conditions will be necessary for all upper-level approximations. Furthermore, implementation of these boundary conditions will have to be carried out while taking into account the additional terms that are produced from their higher-order expansions. For the bidirectional vortex, the first-order counterparts to Eqs. (6–9) may be expressed as:

$$w_1(r,0) = 0; \qquad \frac{1}{r}\frac{\partial \psi_1}{\partial r} - \frac{\rho_1}{r}\frac{\partial \psi_0}{\partial r} = 0 \tag{14}$$

$$u_1(0,z) = 0; \qquad \frac{\rho_1}{r}\frac{\partial \psi_0}{\partial z} - \frac{1}{r}\frac{\partial \psi_1}{\partial z} = 0 \tag{15}$$

$$u_1(1,z) = 0; \qquad \frac{\rho_1}{r}\frac{\partial \psi_0}{\partial z} - \frac{1}{r}\frac{\partial \psi_1}{\partial z} = 0 \tag{16}$$

and

$$2\pi \int_0^\beta (\rho_1 w_0 + w_1)\ r\ \mathrm{d}r = 2\pi \int_0^\beta \frac{\partial \psi_1}{\partial r}\ \mathrm{d}r = 0 \tag{17}$$

These relations represent the first-order constraints for the compressible, bidirectional flowfield. Should higher-order corrections be required, homogeneous constraints that resemble those at the first order could be deployed at $O(M_0^4)$, $O(M_0^6)$, and so on.

III. Compressible Bragg-Hawthorne Formulation

A. Leading-Order Solution

The leading-order stream function must be consistent with the incompressible solution for the same problem. In this spirit, Eq. (1) may be treated with separation of variables.[26] Assuming $\psi_0 = f(r)g(z)$, Eq. (1) becomes

$$-\frac{g''}{g} = \frac{1}{f}\left(f'' - \frac{1}{r}f' + B_0^2 f\right) = \nu^2 \tag{18}$$

where ν^2 can be positive, negative, or zero. Depending on the value chosen for ν^2, three solutions may be conceived, namely,

$$\psi_0 = \begin{cases} r\,(C_1 z + C_2)\,[C_3 J_1(B_0 r) + C_4 Y_1(B_0 r)]\,; & \nu^2 = 0 \\ r\,[C_1 \sin(\nu z) + C_2 \cos(\nu z)]\left[C_3 J_1(r\sqrt{B_0^2 - \nu^2}) + C_4 Y_1(r\sqrt{B_0^2 - \nu^2})\right]; & B_0^2 > \nu^2 \\ r\,[C_1 \sinh(\nu z) + C_2 \cosh(\nu z)]\left[C_3 J_1(r\sqrt{B_0^2 + \nu^2}) + C_4 Y_1(r\sqrt{B_0^2 + \nu^2})\right]; & B_0^2 < \nu^2 \end{cases} \tag{19}$$

In reality, the last two variations prove to be equivalent as one can be reproduced from the other by simply replacing ν with $\pm i\nu$. When accounting for the imaginary part, the hyperbolic functions reduce to their regular trigonometric counterparts as arguments of the Bessel functions become identical when the imaginary ν^2 switches its sign. For brevity, the remainder of this study will focus on the spatially linear case as a vehicle for developing a compressible approximation.

B. Leading-Order Boundary Conditions

To satisfy the centerline boundary conditions for all values of z, we set $C_4 = 0$ everywhere. Furthermore, applying Eq. (6) leads to

$$\frac{\partial \psi_0(r,0)}{\partial r} = C_2 B_0 C_3 J_0(B_0 r) = 0 \tag{20}$$

Since equating either C_3 or B_0 to zero results in a trivial outcome, we take $C_2 = 0$. Substituting the resultant stream function back into the sidewall boundary condition produces

$$\frac{\partial \psi_0(1,z)}{\partial z} = C_3 J_1(B_0) \times \begin{cases} C_1; & \nu^2 = 0 \\ C_1 \nu \cos(\nu z); & \nu^2 \neq 0 \end{cases} \tag{21}$$

For Eq. (21) to be true $\forall z$, B_0 must be a root of the Bessel function of the first kind, or

$$B_0 = \lambda_n; n = 0, 1, 2, \ldots \tag{22}$$

Increments in n will effectively trigger an increasing number of axial reversals in the flow, specifically $(n+1)$ reversals. In practice, only an odd number of reversals will be applicable to the problem at hand and so, to recover the standard bidirectional vortex model,[26] we restrict our analysis to the $n = 0$ case.

At this juncture, we are left with the lumped constant $C_1 C_3$ that must be determined by matching the inflow and outflow mass fluxes. At the leading order, this may be written as

$$2\pi \int_0^\beta \boldsymbol{u} \cdot \boldsymbol{n}\, r \, \mathrm{d}r = 2\pi \int_0^\beta w(r, L)\, r \, \mathrm{d}r = Q_i \tag{23}$$

From the mass balance in Eq. (23) we deduce

$$C_1 C_3 \equiv A_0 = \frac{Q_i}{2\pi\beta L J_1(\lambda_0 \beta)} \tag{24}$$

This converts the stream function form into

$$\psi_0 = A_0 r J_1(\lambda_0 r) \times \begin{cases} z; & \nu^2 = 0 \\ \sin(\nu z); & \nu^2 \neq 0 \end{cases} \tag{25}$$

As to be expected from a leading-order asymptotic approximation, Eq. (25) reproduces the incompressible Beltramian solutions obtained by Majdalani[26] in a right-cylindrical cyclone. With the stream function solution being fully determined, the density may be retrieved from Eq. (3) following a straightforward substitution. After some simplifications, the density may be presented as:

$$\rho_1 = -\frac{A_0^2(\gamma - 1)}{2(\gamma + 1)} \left\{ J_1^2(r\lambda_0) + z^2 \lambda_0^2 \left[J_0^2(r\lambda_0) + J_1^2(r\lambda_0) \right] \right\} \tag{26}$$

Equation (26) is quite illuminating. In fact, it confirms the need for higher powers of ψ within the fundamental definition of B in Eq. (5). Clearly, Bessel functions that are elevated to the second power appear thrice in the density. These, in turn, multiply a single Bessel function in Eq. (2), the first-order stream function relation. In seeking appropriate candidate functions for the particular solution, terms that may be expressed in multiples of three Bessel functions must be attempted. This step is prompted by the requirement to write B in terms of ψ at the basis of the Bragg-Hawthorne procedure.

C. First-Order Stream Function Solution

The first-order correction follows a similar roadmap, albeit with increased complexity. Instead of a homogeneous equation, a particular solution must be determined in such a way to accommodate the terms appearing on the right-hand side of Eq. (2). For the spatially linear case, suitable substitutions of ψ_0 and ρ_1 lead to the first-order, compressible Bragg-Hawthorne equation, namely,

$$\begin{aligned} D^2\psi_1 + B_0^2 \psi_1 = \frac{\gamma - 1}{\gamma + 1} A_0^3 \lambda_0 z J_1(r\lambda_0) \Big(& J_0(r\lambda_0) J_1(r\lambda_0) - 2\lambda_0 r J_0^2(r\lambda_0) \\ & + z^2 \lambda_0^2 \left\{ J_0(r\lambda_0) J_1(r\lambda_0) + r\lambda_0 \left[J_0^2(r\lambda_0) + J_1^2(r\lambda_0) \right] \right\} \Big) - B_2 A_0 r z J_1(r\lambda_0) - B_3 A_0^3 r^3 z^3 J_1^3(r\lambda_0) \end{aligned} \tag{27}$$

Rather than a standard separation of variables approach, we employ an ansatz that is guided by the content of the non-homogeneous terms. Recognizing that both z and z^3 appear in Eq. (27), we let

$$\psi_1 = zR_a + z^3 R_b \tag{28}$$

By virtue of Eq. (28), our single PDE gives rise to two ODEs with one-way coupling through

$$z^3: \; R_b'' - \frac{1}{r}R_b' + \lambda_0^2 R_b = \frac{\gamma-1}{\gamma+1}A_0^3\lambda_0^3 J_1(r\lambda_0)\left\{J_0(r\lambda_0)J_1(r\lambda_0) + r\lambda_0\left[J_0^2(r\lambda_0) + J_1^2(r\lambda_0)\right]\right\} - B_3 A_0^3 r^3 J_1^3(r\lambda_0) \tag{29}$$

$$z: \; R_a'' - \frac{1}{r}R_a' + \lambda_0^2 R_a + 6R_b = \frac{\gamma-1}{\gamma+1}A_0^3\lambda_0 J_1(r\lambda_0)\left[J_0(r\lambda_0)J_1(r\lambda_0) - 2\lambda_0 r J_1(r\lambda_0)\right] - B_2 A_0 r J_1(r\lambda_0) \tag{30}$$

Our next step is to first solve Eq. (29), being a sole function of R_b. The ensuing solution may be then substituted back into Eq. (30) to produce R_a and, with it, a complete compressible correction.

In practice, the solution to Eq. (29) is exacerbated by its dependence on J_0^3 and J_1^3 terms. While Bessel function integrals remain straightforward to evaluate in closed form, integrals for multiplicative Bessel functions can be elusive. In lieu of a completely analytical closure, our correction becomes limited to a semi-analytical formulation that requires the numerical evaluation of a handful of integrals. To overcome, this difficulty, the integrals themselves will be isolated and specified as functions that may be differentiated or integrated at will, so that the boundary conditions can still be determined analytically. In essence, these new integrals may be viewed as special functions that enable us to retain the analytical character of our formulation. After some effort, the z^3 multiplier is found to be

$$\begin{aligned} R_b = {} & rJ_1(r\lambda_0)\left[\frac{\pi}{2}A_0^3\left(\frac{\gamma-1}{\gamma+1}\lambda_0^3\int_1^r J_1(\lambda_0 r_1)Y_1(\lambda_0 r_1)\left\{-\lambda_0 r_1\left[J_0^2(\lambda_0 r_1) + J_1^2(\lambda_0 r_1)\right]\right.\right.\right. \\ & \left.\left.\left. -J_0(\lambda_0 r_1)J_1(\lambda_0 r_1)\right\}\mathrm{d}r_1 + B_3\int_1^r r_1^3 J_1^3(\lambda_0 r_1)Y_1(\lambda_0 r_1)\,\mathrm{d}r_1\right) + A_{1a}\right] \\ & + rY_1(r\lambda_0)\left[\frac{\pi}{2}A_0^3\left(\frac{\gamma-1}{\gamma+1}\lambda_0^3\int_1^r J_1^2(\lambda_0 r_2)\left\{J_0(\lambda_0 r_2)J_1(\lambda_0 r_2) + \lambda_0 r_2\left[J_0^2(\lambda_0 r_2) + J_1^2(\lambda_0 r_2)\right]\right\}\mathrm{d}r_2\right.\right. \\ & \left.\left. + B_3\int_1^r -r_2^3 J_1^4(\lambda_0 r_2)\,\mathrm{d}r_2\right) + A_{1b}\right] \end{aligned} \tag{31}$$

Here A_{1a} and A_{1b} are integration constants while r_1 and r_2 represent variable substitutions in the radial integrals. In treating the integrals as functions, Eq. (31) may be re-written as

$$R_b = rJ_1(r\lambda_0)\left[\frac{\pi}{2}A_0^3\left(\frac{\gamma-1}{\gamma+1}\lambda_0^3 I_1 + B_3 I_2\right) + A_{1a}\right] + rY_1(r\lambda_0)\left[\frac{\pi}{2}A_0^3\left(\frac{\gamma-1}{\gamma+1}\lambda_0^3 I_3 + B_3 I_4\right) + A_{1b}\right] \tag{32}$$

where I_n represents the n^{th} integral in the first-order solution. For the reader's convenience, these are defined in the Appendix.

The z multiplier may be obtained along similar lines. Inserting Eq. (32) into Eq. (30) yields

$$\begin{aligned} R_a = {} & rJ_1(r\lambda_0)\left[\frac{\pi}{2}A_0\left(\frac{\gamma-1}{\gamma+1}A_0^2\lambda_0\int_1^r J_1(\lambda_0 r_1)Y_1(\lambda_0 r_1)\left\{2\lambda_0 r_1 J_0^2(\lambda_0 r_1) - J_0(\lambda_0 r_1)J_1(\lambda_0 r_1)\right\}\mathrm{d}r_1\right.\right. \\ & \left.\left. + B_2\int_1^r r_1 J_1(\lambda_0 r_1)Y_1(\lambda_0 r_1)\,\mathrm{d}r_1\right) + 3\pi\int_1^r Y_1(\lambda_0 r_1)R_b(r_1)\mathrm{d}r_1 + A_{1c}\right] + rY_1(r\lambda_0)\left[\frac{\pi}{2}A_0\left(\frac{\gamma-1}{\gamma+1}A_0^2\lambda_0\int_1^r J_1^2(\lambda_0 r_2)\right.\right. \\ & \left.\left. \times\left\{J_0(\lambda_0 r_2)J_1(\lambda_0 r_2) - 2\lambda_0 r_2 J_0^2(\lambda_0 r_2)\right\}\mathrm{d}r_2 + B_2\int_1^r -r_2 J_1^2(\lambda_0 r_2)\,\mathrm{d}r_2\right) - 3\pi\int_1^r J_1(\lambda_0 r_2)R_b(r_2)\mathrm{d}r_2 + A_{1d}\right] \end{aligned} \tag{33}$$

Here too, the same nomenclature for the special integrals may be used to turn Eq. (33) into

$$\begin{aligned} R_a = {} & rJ_1(r\lambda_0)\left[\frac{\pi}{2}A_0\left(\frac{\gamma-1}{\gamma+1}A_0^2\lambda_0 I_5 + B_2 I_6\right) + 3\pi I_7 + A_{1c}\right] \\ & + rY_1(r\lambda_0)\left[\frac{\pi}{2}A_0\left(\frac{\gamma-1}{\gamma+1}A_0^2\lambda_0 I_8 + B_2 I_9\right) - 3\pi I_{10} + A_{1d}\right] \end{aligned} \tag{34}$$

By substituting Eqs. (32) and (34) back into Eq. (28), one arrives at the general compressible correction. In what follows, an appropriate set of boundary conditions will be considered and discussed.

D. First-Order Boundary Conditions

Compared to the leading order, the boundary conditions at the first order change slightly. In fact, ensuring that the compressible correction does not unduly influence the solution warrants the use of homogeneous constraints. Because our boundary conditions are written in terms of the velocity, it is useful to revisit the expanded velocity-stream function relationship. At the first order, we have

$$u_1 = \frac{\rho_1}{r}\frac{\partial \psi_0}{\partial z} - \frac{1}{r}\frac{\partial \psi_1}{\partial z} \tag{35}$$

$$w_1 = \frac{1}{r}\frac{\partial \psi_1}{\partial r} - \frac{\rho_1}{r}\frac{\partial \psi_0}{\partial r} \tag{36}$$

To avoid lengthy stream function expressions, we omit the general expansion of Eqs. (35) and (36). Instead, we examine each boundary condition individually. For the centerline condition, we find

$$u_1(0,z) = -3z^2 Y_1(0)\left\{\frac{\pi}{2}A_0^3\left[\frac{\gamma-1}{\gamma+1}\lambda_0^3 I_3(0) + B_3 I_4(0)\right] + A_{1b}\right\} + Y_1(0)\left[\frac{\pi}{2}\frac{\gamma-1}{\gamma+1}A_0^3\lambda_0 I_8(0) + \frac{\pi}{2}A_0 B_2 I_9(0) - 3\pi I_{10}(0) + A_{1d}\right] = 0 \tag{37}$$

In actuality, Eq. (37) gives rise to two distinct equalities that are needed to permit the radial velocity to vanish for all values of z. To this end, coefficients multiplying z^2 and those of $O(1)$ must vanish independently. For the z^2 terms, we recover

$$\frac{\pi}{2}A_0^3\left[\frac{\gamma-1}{\gamma+1}\lambda_0^3 I_3(0) + B_3 I_4(0)\right] + A_{1b} = 0 \tag{38}$$

and, for the z^0 coefficient, we are left with

$$\frac{\pi}{2}\frac{\gamma-1}{\gamma+1}A_0^3\lambda_0 I_8(0) + \frac{\pi}{2}A_0 B_2 I_9(0) - 3\pi I_{10}(0) + A_{1d} = 0 \tag{39}$$

The sidewall boundary condition also separates into a pair of constraints. The resulting relation for the z^2 expression becomes

$$\frac{\pi}{2}A_0^3\left[\frac{\gamma-1}{\gamma+1}\lambda_0^3 I_3(1) + B_3 I_4(1)\right] + A_{1b} = 0 \tag{40}$$

and, similarly, at $O(1)$ we retrieve

$$\frac{\pi}{2}\frac{\gamma-1}{\gamma+1}A_0^3\lambda_0 I_8(1) + \frac{\pi}{2}A_0 B_2 I_9(1) - 3\pi I_{10}(1) + A_{1d} = 0 \tag{41}$$

Realizing that the integrals $I_8(1)$, $I_9(0)$, $I_3(1)$, and $I_4(1)$ vanish identically, A_{1b} and A_{1c} may be fully determined from

$$A_{1b} = 0;\ A_{1d} = 3\pi I_{10}(0) - \frac{\pi}{2}\frac{\gamma-1}{\gamma+1}A_0^3\lambda_0 I_8(0) \tag{42}$$

With A_{1b} and A_{1d} in hand, the B_2 and B_3 constants may be deduced from Eqs. (38) and (39). The resulting operations return

$$B_2 = \frac{2\left[3\pi I_{10}(1) - A_{1d}\right]}{\pi A_0 I_9(1)} \tag{43}$$

$$B_3 = -\lambda_0^3\frac{\gamma-1}{\gamma+1}\frac{I_3(0)}{I_4(0)} \tag{44}$$

Finally, the expanded mass balance condition may be expressed as

$$2\pi\int_0^\beta \left[\rho_1 w_0(r,L) + w_1(r,L)\right]\ r\,\mathrm{d}r = 0 \tag{45}$$

The detailed form of the above expression is prohibitively long and, as such, of minimal interest to the reader. However, the remaining integral may be easily handled using symbolic programming. The evaluation of Eq. (45) completes our analysis of the first-order compressible stream function from which all other flow parameters may be retrieved.

IV. Results and Discussion

A. Compressible Velocity Steepening

Pursuant to the stream function determination, the compressible motion may be characterized in all three spatial directions. To avoid unnecessary collisions and potential recirculations, the open fraction at the base, β, may be conveniently equated to the dimensionless mantle radius with the effect of allowing the outgoing stream to exit the chamber unobstructed. Following Majdalani,[26] we set $\kappa = 1$ to provide a magnified view of the variables of interest without suffering the incumbent reduction in accuracy that can accompany substantial increases in the reference Mach number. To facilitate comparisons relative to previous studies, the aspect ratio of the chamber is taken to be $l = \frac{4}{3}$, while typical values of $\gamma = 1.2$ and 1.4 are assigned to the ratio of specific heats. As for the injection Mach number, we anchor our analysis around $M_0 = 0.1$ and 0.2, being two commonly used values in propulsive applications.

Thus motivated by the need to characterize the VCCWC bulk flowfield, we begin with the axial velocity, w, which drives engine performance after expansion. In Fig. 3a we consider the axial profile at the chamber exit, $z = l$, for reference Mach numbers of 0.1 (blue) and 0.2 (red), and for $\gamma = 1.2$ (dashed), and 1.4 (dotted). At $M_0 = 0.1$, the compressible contribution seems to induce a minor though still visible variation in the velocity profile; however, by increasing the injection speed to $M_0 = 0.2$, a substantially more appreciable effect is realized. These profiles also display a sensitivity to variations in γ. Clearly, increasing γ leads to a flattening of the profile in the inner vortex region. Similarly, along with the growth in the injection Mach number, the axial velocity exhibits a steepening effect. When this occurs, the polarity transition that accompanies mantle formation acquires a blunter slope as w crosses the radial axis vertically. This finding is consistent with the axial steepening observed in compressible models of solid rocket motors (SRMs).[30–33] In contrast to the aforementioned studies, no net-amplification of the axial velocity may be noted, aside from a reshaping of the profile itself. As the conservation constraint at the exit must be completely satisfied at the leading order, the resulting mass exiting the chamber at the first order must be self-canceling when integrated over the flow cross-section. This requirement compels the morphing of the velocity contour without affecting the overall mass flux. As for the compressible contribution w_1 depicted in Fig. 3b, it is featured for the two representative values of γ. Based on the BHE framework, the first-order correction will be more pronounced at higher values of γ, $\forall M_0$. Additionally, it can be seen that the compressible contribution will vanish at two distinct points, namely, $r = 0.2$ and 0.75. These sites derive their location from the mass balance relation which, when applied to the compressible correction, will warrant the existence of two polarity switches in the axial velocity to produce a zero net flux.

By virtue of continuity and momentum balances, elements of the steepening mechanism observed in w are transferred to the radial velocity, u, as shown in Fig. 4a. For small deviations from the incompressible case of $M_0 = 0$, the solution seems to be fairly well guided by the shape of the unperturbed solution. In our case, the effect of compression causes a spatial shifting of the peak magnitude in u towards $r = 1$. As the Mach number is further increased to $M_0 = 0.2$, the outward shift in peak amplitudes is accompanied by a more visible increase $\|u_{max}\|$ beyond its incompressible value. This particular amplification of $\|u\|$ in the vicinity of the sidewall can be so pronounced that it must be offset by an appropriate attenuation of the radial velocity in the core region. The corresponding shift in u that is experienced near the centerline causes the radial velocity profile to switch polarity while returning to

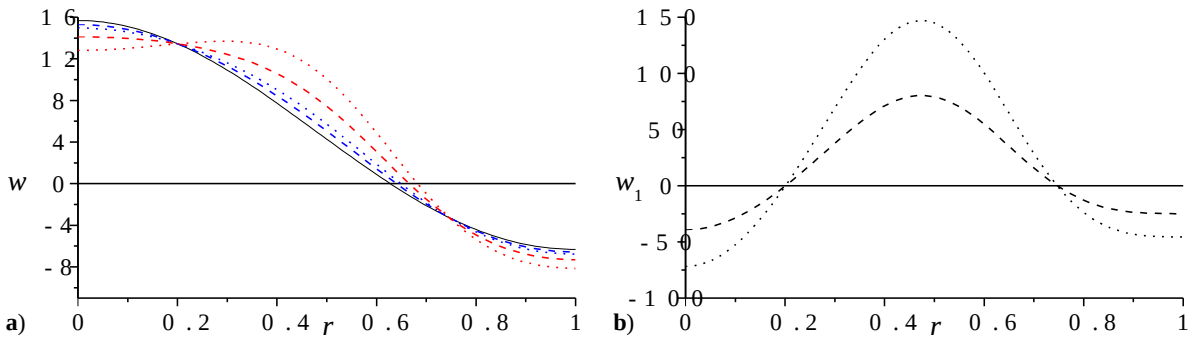

Figure 3. Axial velocity variation in the exit plane showcasing a) the actual profile normalized by κ and b) its compressible correction. Blue and red colors denote in this order the $M_0 = 0.1$ and 0.2 cases. In part a), the solid line stands for the incompressible benchmark, while dashes and dots refer to $\gamma = 1.2$ and 1.4, respectively.

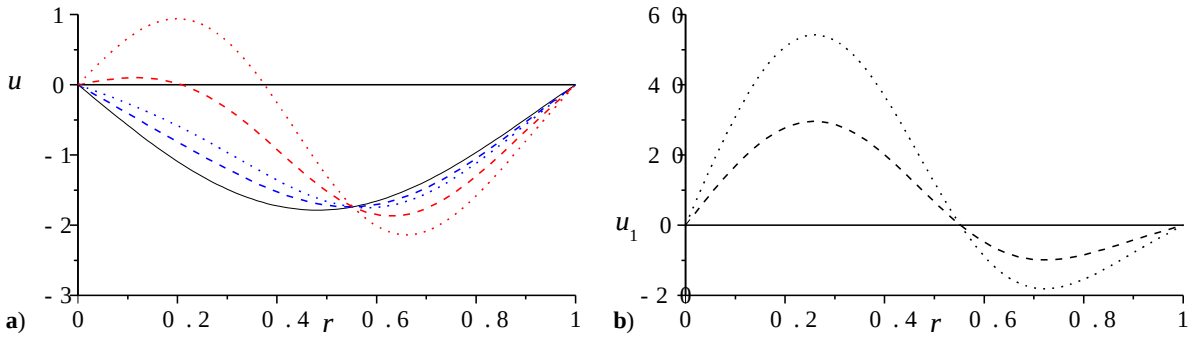

Figure 4. Radial velocity variation in the exit plane showcasing a) the actual profile normalized by κ and b) its compressible correction. Blue and red colors denote in this order the M_0 = 0.1 and 0.2 cases. In part a), the solid line stands for the incompressible benchmark, while dashes and dots refer to γ = 1.2 and 1.4, respectively.

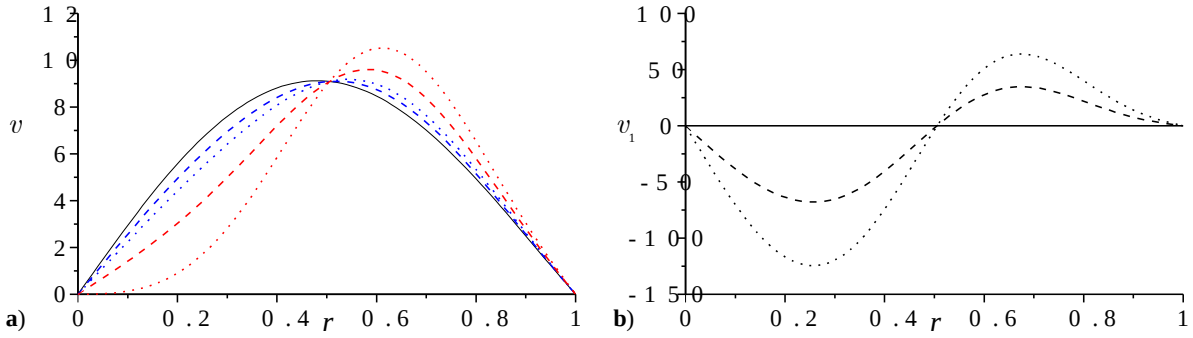

Figure 5. Tangential velocity variation in the exit plane showcasing a) the actual profile normalized by κ and b) its compressible correction. Blue and red colors denote in this order the M_0 = 0.1 and 0.2 cases. In part a), the solid line stands for the incompressible benchmark, while dashes and dots refer to γ = 1.2 and 1.4, respectively.

$r = 0$. Mathematically, because the radial velocity is written as a z derivative of the stream function, it will be strongly influenced by the reversing nature imposed by the conservation principle in the exit plane. Here too, the compressible radial contribution vanishes at $r = 0.55$ as clearly depicted in Fig. 4b. Even for $\kappa = 1$, the total radial velocity remains significantly smaller than the axial or tangential velocities, and this may be attributed to the sidewalls being non-injecting. Nonetheless, the compressible correction itself becomes of the same order in both axial and radial directions, hence leading to a proportionately larger effect on the radial velocity. This behavior will be reversed, however, when κ is reduced in a manner to mitigate the actual compressible contribution.

The third, and most prominent component of the compressible velocity is illustrated in Fig. 5a for the same two Mach numbers and ratios of specific heats. In comparison to u and w, the behavior of the swirl velocity v seems to mimic that of its radial counterpart; its profile is pushed closer to the sidewall with each additional growth in M_0 and γ. Here too, the maximum swirling speed increases at higher values of the Mach number and the specific heats ratio. In Fig. 5b, only the compressible correction is featured for $\gamma = 1.2$ and 1.4. In both cases, the compressible correction vanishes at $r = 0.5$. A closer look at v_1 reveals that its shape resembles that of the radial profile, except for being strictly positive for $0 < r < 1$. Mathematically, differences in magnitudes between u and v may be attributed to the reduced z dependence of the radial velocity, when written in terms of z derivatives, contrary to the swirl velocity v that retains the full z^3 dependence through the stream function expression to which it is linked.

B. Compressible Sliding of the Mantle Interface

One interesting feature of the compressible solution stems from its mantle gaining an axial dependence that cannot be accounted for by the incompressible model. At the leading order, the mantle maintains a constant radial position for all values of z at approximately $r = 0.627$. In the compressible model, the mantle location gains a z dependence

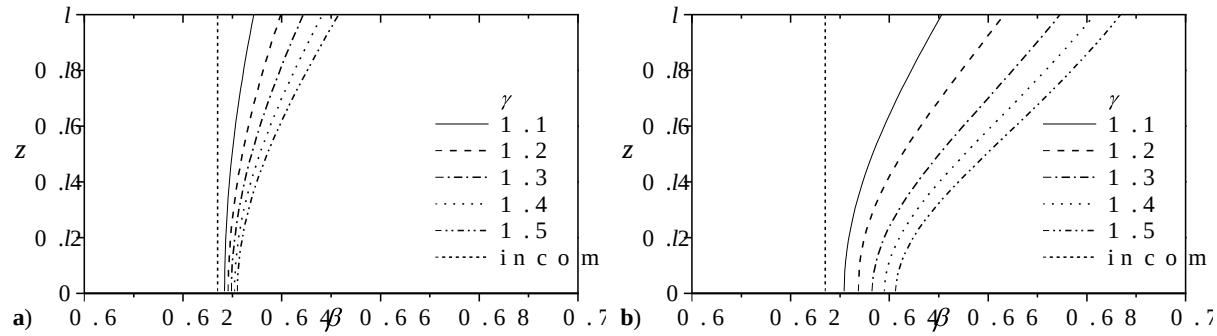

Figure 6. Compressible mantle location for a) M_0 = 0.1 and b) 0.2 using γ = 1.1, 1.2, . . ., 1.5. The vertical line corresponds to the fixed mantle site associated with the incompressible model.

that is clearly illustrated in Fig. 6 for several representative values of the Mach number and γ. Accordingly, the mantle is seen to shift outwardly to a value of 0.639 in the proximity of the headwall ($z = 0$). Then as the fluid travels towards the exit plane, the mantle continues to slide outwardly, almost linearly in z, until reaching a value of 0.681 at $z = l$. Such behavior appears to be consistent with previous theoretical findings based on an entirely different compressible flow approach.[25] At first glance, the linear character of the mantle translation away from the headwall may be viewed as somewhat perplexing because of the solution's explicit dependence on z^3. However, in our situation, the low aspect ratio of $l = \frac{4}{3}$ may be responsible for the linear behavior up to the exit plane. In longer chambers, it is quite likely for the linear behavior to become superseded by a cubic dependence, especially in the presence of sufficiently large reference Mach numbers.

In what concerns experimental evidence, Smith[9,10] reports two antithetical cases, one in which the mantle slides inwardly, towards the centerline, as the distance from the headwall is increased, and one expanding outwardly, towards the sidewall. Without further scrutiny, it may only be possible to speculate over the factors leading to mantle variability. For example, it may be conceivable for viscous effects to compete with compressibility to the extent of one overpowering the other in a given configuration. It is more likely, however, for the geometric design along with its inlet and outlet arrangements to influence the stable position of the mantle interface between the inner and outer vortex regions.[34,35] The presence of a protrusion into the flow, such as the submerged vortex finder appearing in Smith's experiments,[9,10] may have an appreciable bearing on the final mantle location.

C. Density and Pressure Variations

In the compressible Bragg-Hawthorne framework, all thermodynamic quantities may be restored from the density. In view of the isentropic relation used at the basis of the density-stream function formulation, the pressure and temperature may be straightforwardly deduced from the density. With this in mind, retrieving and characterizing the compressible density correction is paramount to the determination and analysis of the corresponding pressure and temperature fields. Both p_1 and T_1 differ from ρ_1 by a constant multiplier, namely,

$$p_1 = \gamma\rho_1 \quad \text{and} \quad T_1 = (\gamma - 1)\rho_1 \tag{46}$$

In Fig. 7, density variations are shown in the exit plane for the two representative injection Mach numbers of M_0 = 0.1 and 0.2, using $\kappa = 1$ and a set of increasing values of $\gamma = 1.1, 1.2, \ldots, 1.5$. As it may be surmised from the graphs, the density appears to be sensitive to both variations in the Mach number and the specific heats ratio. However, the sensitivity to γ is amplified substantially when the Mach number is incremented from 0.1 to 0.2. This may be attributed to the former being closer to the leading-order benchmark than the latter. In any case, as the Mach number and γ are augmented, the normalized density undergoes successive decreases throughout the chamber, with the most significant depreciation occurring along the centerline. It is this particular drop in density that drives, in part, the variation in the axial velocity correction at the first order through its contribution to the mass conservation requirement at $z = l$.

As for the pressure companion, similar trends are depicted in Fig. 8, where the dimensionless pressure distribution is displayed for the same representative values used to analyze the density. Here too, the largest depreciation in the pressure is realized near the centerline, and this effect is accentuated at higher values of M_0 or γ. In the $M_0 = 0.2$ case, the compressible correction causes the pressure near the centerline to drop precipitously, leading to low suction

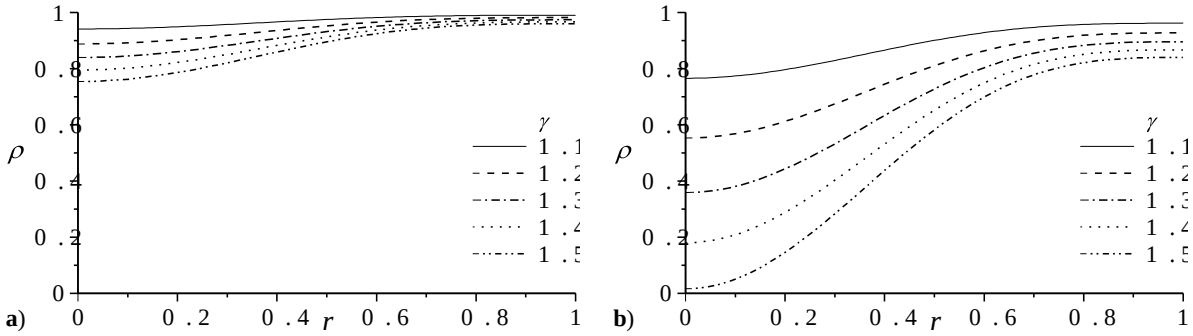

Figure 7. Density distribution for injection Mach numbers of a) $M_0 = 0.1$ and b) 0.2 using $\kappa = 1$, $z = l$, and $\gamma = 1.1, 1.2, \ldots, 1.5$.

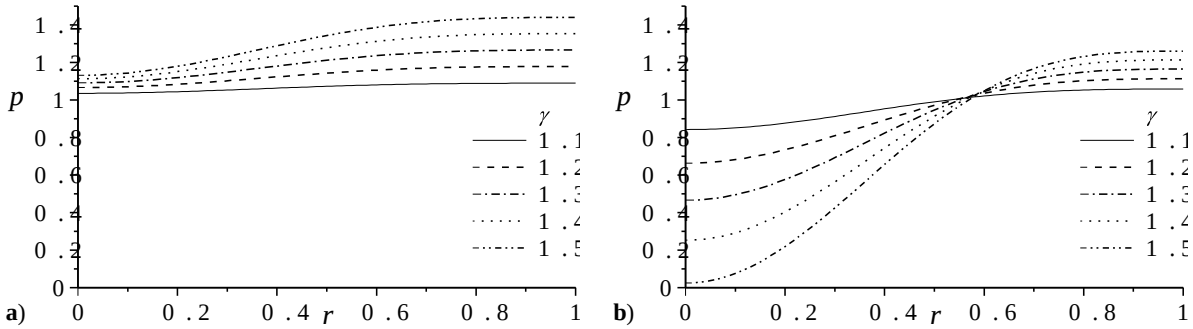

Figure 8. Pressure distribution for injection Mach numbers of a) $M_0 = 0.1$ and b) 0.2 using $\kappa = 1$, $z = l$, and $\gamma = 1.1, 1.2, \ldots, 1.5$.

conditions that become even more pronounced with successive increases in M_0 or γ. At this point, it may be useful to recall that, for cyclonic motion to be stable, the upward streaming of the incoming fluid through a siphoning process is necessary to avoid premature short-circuiting or early spillage out of the open base. It can hence be seen that suction conditions near the centerline can be beneficial to the proper and stable formation of a bidirectional vortex. In consequence, one may conclude that increasing the injection Mach number or the ratio of specific heats will enhance the suction level in the core region, a condition that can lead to a more stable cyclonic flowfield.

D. Sensitivity to the Inflow Swirl Parameter κ

Up to this point, the foregoing solutions have been evaluated for a unit value of κ. This convention has enabled us to amplify the effects of compressibility to the extent of better isolating and capturing the specific features associated with each variable of interest. Realistically speaking, it is possible for κ to take on smaller values, and these will lead to a reduction in the compressible axial and radial speeds alongside their compressible counterparts relative to the tangential velocity. From this perspective, the sensitivity of the compressible approximation to variations in κ can be essential to explore.

To study this sensitivity, the axial velocity profile is re-examined at $z = l$, $\gamma = 1.4$, and both $M_0 = 0.1$ and 0.2. This is accomplished over a range of κ extending from 0.125 to 0.75 as depicted in Fig. 9. It may be safely argued that the remaining dynamic and thermodynamic quantities will exhibit similar trends by virtue of their sensitivity to the swirl parameter κ being analogous to that of the axial velocity. As clearly illustrated on these graphs, decreasing κ leads to a corresponding drop in both compressible and incompressible parts of the axial velocity. The compressible contributions diminish even more rapidly, owing to their cubic dependence on κ, to the extent of approaching the incompressible approximation. Conversely, increasing the injection Mach number to 0.2 or higher stands to offset the effect of decreasing κ.

At low values of κ, the axial and radial velocities, which can directly absorb the effects of compression in the absence of restrictions in the z and r directions, become overwhelmingly dominated by the tangential motion. Their

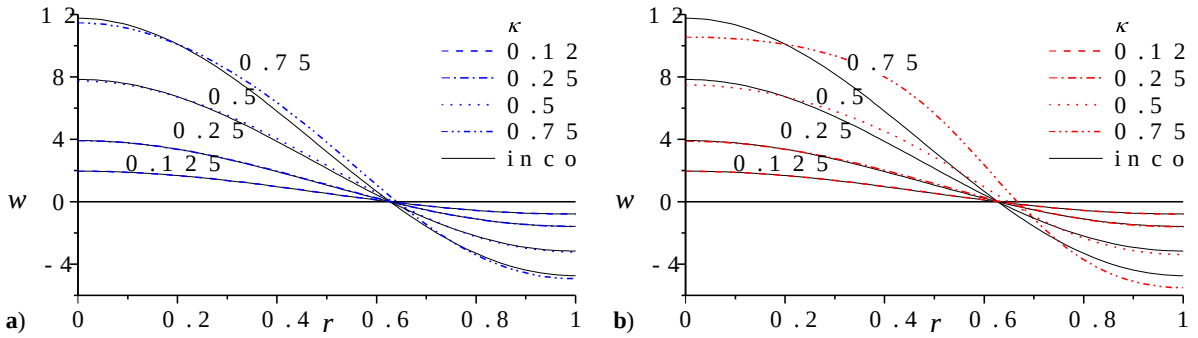

Figure 9. Sensitivity of the axial velocity in the exit plane for injection Mach numbers of a) M_0 = 0.1 and b) 0.2 using κ = 0.125, 0.25, 0.5, and 0.75. The incompressible benchmark uses κ = 1.

overall magnitudes become small relative to v. The latter cannot experience compression in the tangential direction without violating the condition of axisymmetry. Its sensitivity to density variations can only be realized through its spatial dependence on the first-order stream function, and this association is commensurate with the size of both κ and M_0. Naturally, this coupling weakens at decreasing values of κ which, physically, imply the existence of higher levels of swirl and, therefore, stronger tendency to promote an axisymmetric distribution of flowfield properties. So while higher orders of swirl increase the resistance to compression in the tangential direction, higher injection Mach numbers serve to counterbalance this effect, with the overall motion being controlled almost exclusively by these two contending factors. This behavior seems to support the tradition of relying on incompressible models for mean flow Mach numbers below 0.3 irrespective of the flow detail.

V. Concluding Remarks

In this two-paper series, we revisit an important though often overlooked framework in fluid mechanics, namely, a differential technique that is based on the Bragg-Hawthorne or Squire-Long equation. This technique was originally developed to facilitate the modeling of axisymmetric, bathtub-like vortices with intense rotation along their primary axes. The equation itself proceeds from a vorticity-stream function transformation of Euler's inviscid equations into a single, second-order PDE with two principal functions: B, the tangential angular momentum, and H, the stagnation enthalpy or pressure head. In past research, this equation has been explored in a multitude of physical settings, mainly in the treatment of bathtub-like helical structures exhibiting strong axisymmetries. However, these studies have been mostly limited in scope to inviscid and incompressible conditions.

Initially, we have been motivated by a propulsion related study, namely, by the need to describe the internal gas dynamics within a self-cooled thrust chamber wherein the propellant is compelled to follow a cyclonic flowpath. At the outset, we have carried out a two-part investigation aimed, first, at developing a viable mathematical framework and, second, at using this framework to obtain a compressible, inviscid, steady-state approximation for a cylindrical cyclone. In the first part, we have concentrated on producing the compressible analog of the Bragg-Hawthorne approach by deriving, under isentropic flow conditions, the compressible form of the Bragg-Hawthorne equation. By making use of the isentropic pressure-density relation, the stagnation enthalpy expression was employed to achieve the desired closure and, as such, establish the foundation for a well-posed paradigm consisting of two PDEs for the stream function and density. This effort gave rise to a general BHE framework in the form of a density-stream function formulation with the freedom to select B and H and, as usual, the specific boundary conditions for the problem in question. Despite the ability to solve the resulting PDEs by computer, we have opted to linearize them asymptotically for the wide class of problems in which a reference Mach number, M_0, could be designated as a primary perturbation parameter. Thus using the Rayleigh-Janzen perturbation technique known for its relevance to high speed flow applications, the compressible BHE framework was expanded asymptotically and linearized into several pairs of coupled PDEs of increasing order in M_0^2. In theory, the expanded equations could be retrieved to any desired order, thus granting our approach the ability to achieve an arbitrary level of precision. More importantly perhaps, it provided a clear roadmap for producing analytical approximations to a wide range of fluid motions in which density variations may be appreciable.

In this second part, we have focused on the application of this relatively untested framework to a specific profile of the confined bidirectional vortex. For this purpose, we have considered the so-called linear Beltramian model of the cyclonic flowfield arising in the context of a swirl-driven, VCCWC thrust chamber. This particular model has been shown to exhibit features that are appropriate of several laboratory experiments and numerical simulations of the VCCWC prototype and of similarly configured cyclone separators. It has also been derived directly from the incompressible form of the Bragg-Hawthorne equation in cylindrical coordinates.

As may be characteristic of any new approach, the actual application was met by several obstacles that had to be first identified and then overcome. In our case, we have determined that the proper specification of B and H will be quintessential for achieving a well-conceived expansion at the forefront of the analysis. Otherwise, balancing asymptotic terms at successive orders would not be possible. Furthermore, we have realized that the choices leading to an incompressible solution cannot be employed in the compressible framework without judicious modification. Although the incompressible guess function may provide a suitable seed or leading-order start of an expansion, it must be carefully augmented by terms that stem from the particular solutions of the non-homogenous PDEs. In the present work, we provide several guidelines for choosing B and H along with potentially useful series expansions in terms of the reference Mach number.

Thus given a well-balanced procedure, the next challenge stands in resolving the boundary conditions appropriately. This aspect we find to be rather straightforward, especially that the conventional constraints associated with the bidirectional vortex appear (and are hence secured) at the leading order. In consequence, corrections of order one and higher inherit strictly homogenous conditions. When these conditions are systematically used to supplement the linearized density-stream function PDEs at each asymptotic level, a perturbation approximation of increasing accuracy can be achieved by solving the resulting sets of equations in ascending order. The remaining effort is facilitated by taking into account the one-way coupling that exists between the principal PDEs at successive orders. This enables us to solve for one function exclusively before substituting its outcome into the other. The analysis is also simplified by lumping analytically intractable integrals into special functions that can be carried conveniently throughout the derivation. Isolating these integrals not only reduces the algebra involved, but it permits the direct evaluation of boundary conditions and, as such, the attainment of a closed-form approximation. Finally, in view of the size of M_0, we find that a first-order correction is sufficient to capture the bulk effects of fluid dilatation.

The characterization of the compressible Beltramian motion leads to quite interesting and rich patterns. In summary, we find that increasing either the injection Mach number or, to a lesser extent, the ratio of specific heats, will trigger a steepening effect with respect to the incompressible flow analog. This steepening mechanism is accompanied by a sharp density expansion near the axis of rotation and an outward shifting of the mantle interface which separates the outer and inner vortex regions. At the outset, the annular region through which the incoming stream is funneled into the chamber undergoes a constriction in its cross-sectional area. This pinching of the outer vortex is akin to the behavior exhibited by the annular region of the Vortex Injection Hybrid Rocket Engine (VIHRE)[36] as a reaction to increasing the burning rate along its sidewall.[37] Despite the model being incompressible, augmenting the injection mass flow rate within the outer annulus (by virtue of distributed mass addition along the sidewall) forces the mantle to slide outwardly. This outward movement is needed to increase the radius of the inner vortex in such a way to permit more mass to exit the chamber. In the compressible Beltramian case, a similar mechanism is observed and this may be attributed to the density stratification that is induced by fluid compression in conjunction with the presence of strong radial gradients; these give rise to a higher density fluid in the outer vortex and a markedly lower density within the chamber core. Clearly, increasing the fluid density in the annular region is somewhat equivalent to increasing the mass flux locally. Both actions lead to a widening of the outlet section, an outward shifting of the mantle, and a corresponding redistribution of the velocity profiles. For $M_0 = 0.2$, the mantle starts with a radius of 0.639 at the headwall, and then shifts progressively to 0.681 in the exit plane. While a similar steepening due to compressibility has been noted in SRM internal ballistics,[30–32] the flattening of the Beltramian core profile remains spatially restricted; it follows a redistribution that enables the motion to still satisfy the conservation condition imposed at the inflow-outflow boundary in the exit plane.

In addition to the steepening caused by successive increases in the Mach number, our study shows that higher values of M_0 lead to lower pressures in the core region. These, in turn, can promote a stronger siphoning process through which a more effective flow streaming towards the headwall is promoted along with a more stable development of cyclonic motion. Finally, our sensitivity analysis seems to reveal a trade-off between the injection Mach number and the inflow swirl parameter κ. Due to the inability of an axisymmetric flowfield to experience density variations in the θ direction, lower values of κ can suppress the effects of fluid compression by reducing the relative contributions of the axial and radial velocities. Such would be the outcome unless κ is offset by a sufficiently large Mach number.

In closing, we reaffirm that the study presented here is not meant to be a comprehensive investigation of the compressible Bragg-Hawthorne equations. Our framework seems to be viable for a wide range of problems encompassing both confined and unconfined vortex flows. In the case of the bidirectional vortex, other candidate functions for B and H may be chosen to the extent of producing alternate models for the VCCWC internal flowfield. While the present analysis focuses on the spatially linear solution to the stream function equation, it can be suitably extended to the axially trigonometric, nonlinear Beltramian case.

Appendix

This section enumerates a set of integrals that are defined as special functions of the form I_n. These arise in the analysis leading to the compressible first-order formulation of the linear Beltramian flowfield. The specification of the ensuing integrals in terms of simple functions enables us to reduce the first-order equations to a more manageable size and to implement the boundary conditions more expeditiously. Each of these integral functions is delineated as follows:

$$I_1 = \int_1^r J_1(\lambda_0 r_1)\, Y_1(\lambda_0 r_1) \left\{-\lambda_0 r_1 \left[J_0^2(\lambda_0 r_1) + J_1^2(\lambda_0 r_1)\right] - J_0(\lambda_0 r_1)\, J_1(\lambda_0 r_1)\right\} \mathrm{d}r_1 \tag{47}$$

$$I_2 = \int_1^r r_1^3 J_1^3(\lambda_0 r_1)\, Y_1(\lambda_0 r_1)\, \mathrm{d}r_1 \tag{48}$$

$$I_3 = \int_1^r J_1^2(\lambda_0 r_2) \left\{J_0(\lambda_0 r_2)\, J_1(\lambda_0 r_2) + \lambda_0 r_2 \left[J_0^2(\lambda_0 r_2) + J_1^2(\lambda_0 r_2)\right]\right\} \mathrm{d}r_2 \tag{49}$$

$$I_4 = -\int_1^r r_2^3 J_1^4(\lambda_0 r_2)\, \mathrm{d}r_2 \tag{50}$$

$$I_5 = \int_1^r J_1(\lambda_0 r_1)\, Y_1(\lambda_0 r_1) \left\{2\lambda_0 r_1 J_0^2(\lambda_0 r_1) - J_0(\lambda_0 r_1)\, J_1(\lambda_0 r_1)\right\} \mathrm{d}r_1 \tag{51}$$

$$I_6 = \int_1^r r_1 J_1(\lambda_0 r_1)\, Y_1(\lambda_0 r_1)\, \mathrm{d}r_1 \tag{52}$$

$$I_7 = \int_1^r Y_1(\lambda_0 r_1)\, R_b(r_1) \mathrm{d}r_1 \tag{53}$$

$$I_8 = \int_1^r J_1^2(\lambda_0 r_2) \left\{J_0(\lambda_0 r_2)\, J_1(\lambda_0 r_2) - 2\lambda_0 r_2 J_0^2(\lambda_0 r_2)\right\} \mathrm{d}r_2 \tag{54}$$

$$I_9 = -\int_1^r r_2 J_1^2(\lambda_0 r_2)\, \mathrm{d}r_2 \tag{55}$$

$$I_{10} = \int_1^r J_1(\lambda_0 r_2)\, R_b(r_2) \mathrm{d}r_2 \tag{56}$$

Acknowledgments

This material is based on work supported partly by the National Science Foundation and partly by the University of Tennessee Space Institute.

References

[1]Penner, S. S., "Elementary Considerations of the Fluid Mechanics of Tornadoes and Hurricanes," *Acta Astronautica*, Vol. 17, 1972, pp. 351–362.

[2]Königl, A., "Stellar and Galactic Jets: Theoretical Issues," *Canadian Journal of Physics*, Vol. 64, No. 4, 1986, pp. 362–368. doi:10.1139/p86-063.

[3]Bruce, C. E. R., "Spiral Stellar Nebulae and Cosmic Gas Jets," *Journal of the Franklin Institute*, Vol. 271, No. 1, 1961, pp. 1–11. doi:10.1016/s0016-0032(61)91011-0.

[4]Leibovich, S., "The Structure of Vortex Breakdown," *Annual Review of Fluid Mechanics*, Vol. 10, 1978, pp. 221–246. doi:10.1146/annurev.fl.10.010178.001253.

[5]Leibovich, S., "Vortex Stability and Breakdown: Survey and Extension," *AIAA Journal*, Vol. 22, No. 9, 1984, pp. 1192–1206. doi:10.2514/3.8761.

[6]Escudier, M. P., "Vortex Breakdown - Observations and Explanations," *Progress in Aerospace Sciences*, Vol. 25, No. 2, 1988, pp. 189–229. doi:10.1016/0376-0421(88)90007-3.

[7]ter Linden, A. J., "Investigations into Cyclone Dust Collectors," *Proceedings of the Institution of Mechanical Engineers*, Vol. 160, 1949, pp. 233–255.

[8]Kelsall, D. F., "A Study of Motion of Solid Particles in a Hydraulic Cyclone," *Transactions of the Institution of Chemical Engineers*, Vol. 30, 1952, pp. 87–103.

[9]Smith, J. L., "An Experimental Study of the Vortex in the Cyclone Separator," *Journal of Basic Engineering*, 1962, pp. 602–608.

[10]Smith, J. L., "An Analysis of the Vortex Flow in a Cyclone Separator," *Journal of Basic Engineering*, 1962, pp. 609–618.

[11]Hoekstra, A. J., Derksen, J. J., and van den Akker, H. E. A., "An Experimental and Numerical Study of Turbulent Swirling Flow in Gas Cyclones," *Chemical Engineering Science*, Vol. 54, No. 3, 1999, pp. 2055–2065. doi:10.1016/S0009-2509(98)00373-X.

[12]Fang, D., Majdalani, J., and Chiaverini, M. J., "Simulation of the Cold-Wall Swirl Driven Combustion Chamber," *39th AIAA/ASME/SAE/ASEE Joint Propulsion Conference and Exhibit*, AIAA Paper 2004-3359, Huntsville, AL, July 2003.

[13]Rom, C. J., Anderson, M. H., and Chiaverini, M. J., "Cold Flow Analysis of a Vortex Chamber Engine for Gelled Propellant Combustor Applications," *40th AIAA/ASME/SAE/ASEE Joint Propulsion Conference and Exhibit*, AIAA Paper 2004-3359, Fort Lauderdale, FL, July 2004.

[14]Hu, L. Y., Zhou, L. X., Zhang, J., and Shi, M. X., "Studies of Strongly Swirling Flows in the Full Space of a Volute Cyclone Separator," *AIChE Journal*, Vol. 51, No. 3, March 2005, pp. 740–749.

[15]Zhiping, Z., Yongjie, N., and Qinggang, L., "Pressure Drop in Cyclone Separator at High Pressure," *Journal of Thermal Science*, Vol. 17, No. 3, 2008, pp. 275–280. doi:10.1007/s11630-008-0275-7.

[16]Bloor, M. I. G., and Ingham, D. B., "The Flow in Industrial Cyclones," *Journal of Fluid Mechanics*, Vol. 178, 1987, pp. 507–519. doi:10.1017/S0022112087001344.

[17]Barber, T. A., and Majdalani, J., "Exact Eulerian Solution of the Conical Bidirectional Vortex," *45th AIAA/ASME/SAE/ASEE Joint Propulsion Conference and Exhibit*, AIAA Paper 2009-5306, Denver, CO, August 2009.

[18]Cortes, C., and Gil, A., "Modeling the Gas and Particle Flow Inside Cyclone Separators," *Progress in Energy and Combustion Science*, Vol. 33, No. 5, 2007, pp. 409–452. doi:10.1016/j.pecs.2007.02.001.

[19]Vyas, A. B., and Majdalani, J., "Exact Solution of the Bidirectional Vortex," *AIAA Journal*, Vol. 44, No. 10, October 2006, pp. 2208–2216. doi:10.2514/1.14872.

[20]Chiaverini, M. J., Malecki, M. J., Sauer, A., and Knuth, W. H., "Vortex Combustion Chamber Development for Future Liquid Rocket Engine Applications," *38th AIAA/ASME/SAE/ASEE Joint Propulsion Conference and Exhibit*, AIAA Paper 2002-4149, Indianapolis, IN, July 2002.

[21]Vyas, A. B., Majdalani, J., and Chiaverini, M. J., "The Bidirectional Vortex. Part 2: Viscous Core Corrections," *39th AIAA/ASME/SAE/ASEE Joint Propulsion Conference and Exhibit*, AIAA Paper 2003-5053, Huntsville, AL, July 2003.

[22]Vyas, A. B., Majdalani, J., and Chiaverini, M. J., "The Bidirectional Vortex. Part 3: Multiple Solutions," *39th AIAA/ASME/SAE/ASEE Joint Propulsion Conference and Exhibit*, AIAA Paper 2003-5054, Huntsville, AL, July 2003.

[23]Majdalani, J., and Chiaverini, M. J., "On Steady Rotational Cyclonic Flows: The Viscous Bidirectional Vortex," *Physics of Fluids*, Vol. 21, 2009, pp. 103603–15.

[24]Batterson, J. W., and Majdalani, J., "Sidewall Boundary Layers of the Bidirectional Vortex," *Journal of Propulsion and Power*, Vol. 26, No. 1, 2010, pp. 102–112. doi:10.2514/1.40442.

[25]Maicke, B. A., and Majdalani, J., "On the Compressible Bidirectional Vortex," *44th AIAA/ASME/SAE/ASEE Joint Propulsion Conference and Exhibit*, AIAA Paper 2008-4834, Hartford, CT, July 2008.

[26]Majdalani, J., "Exact Eulerian Solutions of the Cylindrical Bidirectional Vortex," *45th AIAA/ASME/SAE/ASEE Joint Propulsion Conference and Exhibit*, AIAA Paper 2009-5307, Denver, CO, August 2009.

[27]Chiaverini, M., Malecki, M., Sauer, J., Knuth, W., and Majdalani, J., "Vortex Thrust Chamber Testing and Analysis for O2-H2 Propulsion Application," *39th AIAA/ASME/SAE/ASEE Joint Propulsion Conference and Exhibit*, AIAA Paper 2003-4473, Huntsville, AL, July 2003.

[28]Chiaverini, M. J., Malecki, M. J., Sauer, J. A., Knuth, W. H., and Hall, C. D., "Final Report on Cold-Wall Vortex Combustion Chamber-a Phase I SBIR Project," NASA Contact No. NAS8-01073 OTC-GS0107-01-1, Orbital Technological Corporation, August 2001.

[29]Maicke, B. A., and Majdalani, J., "On the Compressible Bidirectional Vortex. Part 1: A Bragg-Hawthorne Stream Function Formulation," *50th AIAA Aerospace Sciences Meeting Including the New Horizons Forum and Aerospace Exposition*, AIAA Paper 2012-1103, Nashville, TN, January 2012.

[30]Majdalani, J., "On Steady Rotational High Speed Flows: the Compressible Taylor-Culick Profile," *Proceedings of the Royal Society of London, Series A*, Vol. 463, January 2007, pp. 131–162. doi:10.1098/rspa.2006.1755.

[31]Maicke, B. A., and Majdalani, J., "On the Rotational Compressible Taylor Flow in Injection-Driven Porous Chambers," *Journal of Fluid Mechanics*, Vol. 603, 2008, pp. 391–411. doi:10.1017/S0022112008001122.

[32]Balakrishnan, G., Liñán, A., and Williams, F. A., "Rotational Inviscid Flow in Laterally Burning Solid Propellant Rocket Motors," *Journal of Propulsion and power*, Vol. 8, No. 6, November-December 1992, pp. 1167–1176. doi:10.2514/3.11458.

[33]Saad, T., and Majdalani, J., "On the Lagrangian Optimization of Wall-Injected Flows: From the Hart-McClure Potential to the Taylor-Culick Rotational Motion," *Proceedings of the Royal Society of London, Series A*, Vol. 466, No. 2114, 2010, pp. 331–362. doi:10.1098/rspa.2009.0326, 10.1098/rspa.2009.0326.

[34]Akiki, G., and Majdalani, J., "On the Bidirectional Vortex with Arbitrary Endwall Velocity," *46th AIAA/ASME/SAE/ASEE Joint Propulsion Conference and Exhibit*, AIAA Paper 2010-6652, July 2010.

[35]Akiki, G., and Majdalani, J., "On the Viscous Bidirectional Vortex with Arbitrary Endwall Injection," *47th AIAA/ASME/SAE/ASEE Joint Propulsion Conference and Exhibit*, AIAA Paper 2011-5692, July-August 2011.

[36]Knuth, W. H., Bemowski, P. A., Gramer, D. J., Majdalani, J., and Rothbauer, W. J., "Gas-Fed, Vortex Injection Hybrid Rocket Engine," SBIR Phase I Final Technical NASA/MSFC Contract NAS8-40679, NASA Marshall Space Flight Center, August 1996.

[37]Majdalani, J., "Vortex Injection Hybrid Rockets," *Fundamentals of Hybrid Rocket Combustion and Propulsion*, edited by K. Kuo and M. J. Chiaverini, Progress in Astronautics and Aeronautics, chap. Chap. 6, AIAA Progress in Astronautics and Aeronautics, Washington, DC, 2007, pp. 247–276.